Thin–Walled Structures 198 (2024) 111756

Contents lists available at ScienceDirect

Thin-Walled Structures

journal homepage: www.elsevier.com/locate/tws

Full length article

Band folding induced broadband vibration suppression of star-shaped metamaterials: Theory and experiment

Zhenkun Guo [a], Jiaqi Wen [a,b], Yongjun Shen [c], Guobiao Hu [b,*], Guoqing Jiang [d]

[a] Beijing Engineering Research Center of Monitoring for Construction Safety, Beijing University of Civil Engineering and Architecture, Beijing, 100044, China
[b] Internet of Things Thrust, The Hong Kong University of Science and Technology (Guangzhou), Guangzhou, 511400, China
[c] State Key Laboratory of Mechanical Behavior and System Safety of Traffic Engineering Structures, Shijiazhuang Tiedao University, Shijiazhuang, 050043, China
[d] School of Mechanical Engineering, Zhejiang Sci-Tech University, Hangzhou, 310018, China

ARTICLE INFO

Keywords:
Star-shaped metamaterial
Bandgap
Band folding
Broadband vibration suppression
Truss structures

ABSTRACT

Metamaterials with bandgap features can block wave propagation in specific frequency ranges and thus have wide applications for vibration mitigation and noise reduction. In this study, we renovated the design of star-shaped metamaterial (SSM) to make it capable of producing lower and wider vibration bandgaps. Unlike traditional periodic truss structures in the literature, the designed SSM structure breaks the spatial symmetry, opening the degenerate points formed by the band folding effect, thereby producing extra bandgaps for vibration suppression. First of all, a finite element (FE) model of the SSM is established, and its band structures and vibration transmittance are calculated. The preliminary result validated our hypothesis, demonstrating that the proposed SSM structure created additional bandgaps for suppressing low-frequency and broadband vibrations. Subsequently, the frequency response analyses are conducted using the spectral element method (SEM) and experimental test. The effects of the structural parameters on the bandgaps of the proposed SSM are studied. In addition, we further extended and generalized the band folding design concept. We showed that one can produce more bandgaps by designing high-order SSMs. In general, this study presents an approach for designing truss structures with broadband vibration suppression performance.

1. Introduction

Vibration suppression and noise reduction have always been challenging and pragmatic. In particular, low-frequency, ultra-low frequency, and broadband vibration and noise control are cutting-edge issues that have attracted much research interest. In the past years, innovative approaches have been developed to tackle these challenges, such as using elastic metamaterials. Metamaterials are a unique type of periodic structure with exceptional low-frequency and broadband wave attenuation capabilities. Exploring the mechanical properties and the design of structural units of metamaterials are trending topics in this area [1–5]. Metamaterials presented as artificially designed composite material structures exhibit extraordinary physical properties that natural materials do not have. Researchers found that periodic elastic composite media can create wave bandgaps to block mechanical and/or acoustic waves in specific frequency ranges. Within the bandgap, waves are inhibited from propagating, resulting in spatial isolation of the vibration source and offering a novel dynamic design concept for vibration suppression.

There exist two mechanisms for generating bandgaps, namely Bragg scattering (BS) and local resonance (LR) [6]. The structural periodicity mainly dominates the former one. When the wavelength of the incident elastic wave is close to the characteristic length of the structure, i.e., lattice constant, a strong scattering effect will happen. The local resonances of microstructures mainly dominate the latter one. LR metamaterials break through the limitation of lattice size-dependency. They can be designed in subwavelength scales to control wave propagation, thus providing a theoretical basis for controlling low-frequency vibration. Recently, Guo et al. [7] designed a broadband low-frequency sandwich metamaterial structure with a lattice truss core. Although the LR mechanism can generate low-frequency bandgaps, their complex structures often increase the manufacturing difficulty and cost. Besides, researchers have also developed different nonlinear LR metamaterials to lower the bandgap frequency ranges [8–10]. Xue et al. [11] utilized magnetorheological elastomers as resonators and combined them with periodic springs and levers to achieve broadband adjustment of

* Corresponding author.
E-mail address: guobiaohu@hkust-gz.edu.cn (G. Hu).

https://doi.org/10.1016/j.tws.2024.111756
Received 19 December 2023; Received in revised form 22 February 2024; Accepted 26 February 2024
Available online 27 February 2024
0263-8231/© 2024 Elsevier Ltd. All rights reserved.

nonlinear bandgaps. Based on this, they designed an LR metamaterial plate with frequency feedback to realize the active control of bandgaps [12]. Tian et al. [13] designed springs with tunable nonlinear stiffness to realize nonlinear vibration and flutter suppressions. Based on that, they proposed nonlinear metamaterials improved with the cantilever resonator by combining a rigid cantilever beam and a mass block, which can be used to suppress broadband vibration with multiple modes [14,15]. Besides, researchers introduced some innovative structures with unique properties into the design of LR metamaterials, including negative stiffness structures [16,17], membrane-type structures [18], and origami structures [19] etc., to obtain lightweight structures having exceptional vibration suppression performance. In brief, resonators need to be added to the LR metamaterials, which unavoidably changes the mechanical properties of the substrate structure.

Star-shaped structures with double-negative characteristics have drawn the attention of many scholars. Chen et al. [20] demonstrated that star-shaped periodic structures possess negative Poisson's ratios. Moreover, they exhibit high design flexibility, are lightweight, and have superior energy absorption efficiencies. In addition, they can generate low-frequency bandgaps and display extraordinary dynamic characteristics due to their concave configurations. Meng et al. [21] analyzed the equivalent mechanical behavior and bandgap characteristics of star-shaped honeycombs. Their results showed the existence of much lower frequency bandgaps. Star-shaped structures belong to truss structures, typically comprised of slender beams and/or rods. Truss structures are widely used in industries because of their high stiffness/strength, uniform internal force distribution, and excellent lightweight properties. In the dynamic modeling of truss structures, it is essential to account for the axial force, torsional force, and transverse shearing force of the beam/rod elements to ensure accuracy. Various methods have been developed to study the bandgap characteristics of truss structures. Wu et al. [22,23] established dynamic models of two-dimensional (2D) and three-dimensional (3D) periodic truss structures using the spectral element method (SEM). The troughs presented in the frequency response curves in their results revealed the BS bandgap in the high-frequency region. Zuo et al. [24] verified the existence of vibration bandgaps in planar periodic rigid frame structures using experimental testing methods. Lu et al. [25] designed functionally graded frame structures to produce wider bandgaps than traditional homogeneous truss structures. The transfer matrix method (TMM) is also a classic theoretical method for the dynamic modeling of periodic truss structures. The TMM method can be conveniently combined with Bloch's theorem to analyze the dispersion relationship and identify bandgaps [26]. Moreover, Phani et al. [27] studied the plane wave propagation in infinite 2D periodic lattices using Bloch's theorem. They used the finite element method (FEM) to model the unit cell of each lattice and obtained the band structures by solving the eigenvalue problem of wave propagation. The acoustic black hole theory has also been employed by scholars to design V-folded beam structures to achieve the coupling of flexural wave and longitudinal wave, which makes the elastic wave greatly attenuated [28].

In condensed matter physics, the discovery of the Hall effect has led to the development of topological matter physics [29]. Periodicity and Bragg scattering make the energy show a band distribution. The band structure of graphene is observed to be conical in its Brillouin zone [30], the intersection of the bands is defined as the Dirac point, and the dispersion near it is linear. Haladane and Raghu [31,32] used the Faraday effect medium to break the time inversion symmetry to open the Dirac point and obtain a bandgap. In addition, opening the band degeneracy point can also be achieved by breaking the spatial symmetry [33]. Besides, He et al. [34] found that the band inversion was achieved by regulating the double Dirac points that were assumed to degenerate, and the acoustic quantum spin Hall effect was realized. The researchers realized the topological transformation process of the Dirac point from degeneracy to opening (band from opening to closing and then to opening) by adjusting the duty ratio in the unit cell of a 2D honeycomb lattice metamaterial. Inspired by the previous works, Zhang et al. [35] designed a 3D magnetoelastic topological insulator with controllable working frequency and wave propagation path by adjusting the applied magnetic field or prestress. They managed to break the spatial symmetry, realized the topological phase transition, and opened the Dirac point to form an extra bandgap. Huang et al. [36] designed a multi-band topological insulator by using the lattice superposition mechanism and summarized a general method for realizing multiple degeneracies in the center of the Brillouin zone.

In summary, although the dynamics and bandgap behaviors of star-shaped structures have been studied by researchers, achieving low-frequency broadband vibration suppression by traditional periodic star-shaped structures remains a challenge. Therefore, this paper proposes a novel star-shaped structure, referred to as star-shaped metamaterial (SSM), with each unit cell comprising two alternating substructures with different concave angles. The band structure and frequency response analyses demonstrate that the SSM structure can generate more bandgaps than traditional ones in the low-frequency regime for broadband vibration suppression. Subsequently, theoretical models are developed, and experimental tests are conducted to verify the correctness of the results by FEM. Based on the theoretical model, the effects of structural parameters and the folding order on the bandgap formation of the proposed SSM structure are also revealed.

2. Design and mechanism of the proposed SSM

The proposed SSM is composed of lightweight star-shaped truss structures and can generate extra bandgaps by breaking spatial symmetry. The design strategy utilized in this star-shaped structure presents a new design method for lightweight acoustic lenses, wave filters, and vibration isolation infrastructures [20,37]. This section describes the structural design of SSM. The band structures analysis shows that the proposed SSM can generate lower frequency and broadband bandgaps compared with the conventional one. The mechanisms of band folding and extra bandgap formation are explained. Additionally, vibration transmittance analysis is conducted to confirm the band structure results.

2.1. Overview of the SSM structure

The proposed SSM structure comprises periodically arranged unit cells, viz. representative volume elements (RVEs). The RVE consists of two star-shaped substructures with different concave angles. As shown in Fig. 1(a), each substructure consists of ten struts with the same elasticity, uniformity, and isotropy. The strut length of the first substructure in the unit cell is denoted by L_1, and the strut length of the second substructure is denoted by L_2. The concave angles of the two substructures are denoted by α and β, respectively. Considering the geometric characteristics of the star-shaped structure, α and β take values between 45°and 90°. Thus, the lattice constant of the SSM can be calculated as $a = L_1 \times [1\text{-}\cos(\alpha)+\sin(\alpha)] + L_2 \times [1\text{-}\cos(\beta)+\sin(\beta)]$. The square cross-sectional area $A = b \times b$ of the struts is shown in Fig. 1(b), where b denotes the side length. By periodically arranging unit cells in the x-direction, the schematic diagram of an infinite SSM can be obtained, as shown in Fig. 1(c).

2.2. Band structure analysis

The SSM proposed in this paper consists of unit cells periodically distributed along the x-direction. By using FEM, which assumes that the band structure is calculated by the perfect phononic crystal structure with an infinite period, the dispersion relation of the SSM can be obtained. For the one-dimensional (1D) lattice, there is no corresponding reduced Brillouin zone, the length of the primitive cell basis vector **a** is lattice constant a, and the length of the inverted lattice basis vector **b** is $2\pi/a$. For the unit cell with periodic boundary conditions in the x-

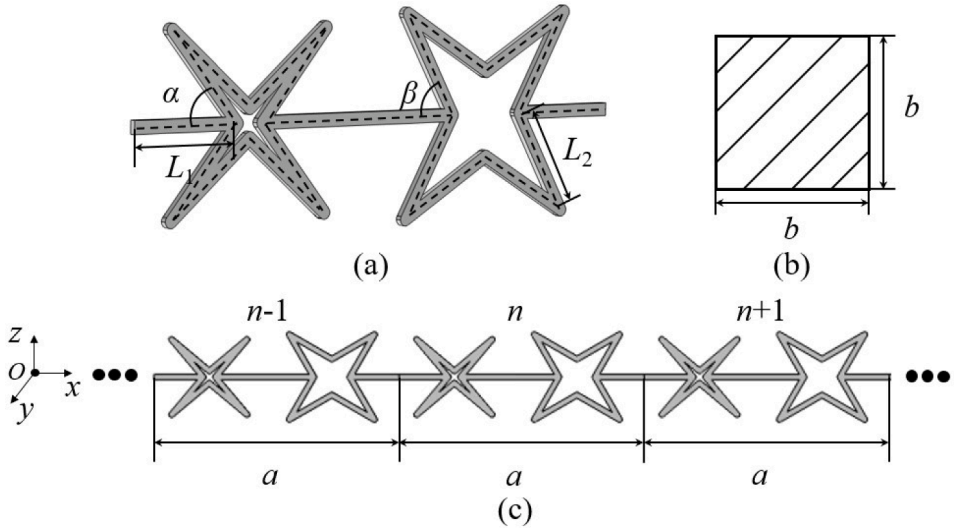

Fig. 1. Schematic of the (a) SSM unit cell, (b) cross-section of the struts, (c) infinite SSM structure.

direction, the wave propagating in the lattice periodic medium is a plane wave modulated by the lattice periodicity based on the Floquet-Bloch theorem. The Bloch periodic condition can be applied to the two boundaries of the unit cell in the x-direction as

$$u(m+r) = u(m)e^{-ik_x m} \tag{1}$$

where $u(\mathbf{m})$ represents the longitudinal displacement, $\mathbf{m}$ represents the position vector, $\mathbf{r}$ represents the basis vector of the lattice, i represents the imaginary number, k_x represents the wave vector component along the x-direction. Therefore, by sweeping k_x, the eigenvalue equation that relates the natural frequency and the wave vector can be obtained. The band structures can be plotted by deeming the natural frequency as a function of the wave vector and solving the corresponding eigenvalue problem. For the subsequent calculation and comparison of band structures, Fig. 2(a) and (b) respectively show diagrams of the traditional star-shaped structure monoatomic unit cell and diatomic unit cell with concave angle Φ, and Fig. 3(c) shows diagram of the SSM unit cell.

Given the parameters in Table 1, the dispersion curves of the SSM are plotted in Fig. 3(d). Besides, given the same parameters as listed in Table 1, the monoatomic unit cells with $\Phi = 50^{\circ}$ and $\Phi = 60^{\circ}$ are also analyzed, and their dispersion curves are shown in Fig. 3(a) and (b). On this basis, we considered an enlarged unit cell (a diatomic unit cell) with $\Phi = 50^{\circ}$. From Fig. 3(c), it can be observed that the band folding phenomenon occurs, and two degenerate Dirac points A and B are generated [38,39]. In fact, comparing Fig. 3(a) and (c), one can note that the bands are folded back due to the folding of the reciprocal space. Once we transform the enlarged unit cell into a real primitive one by making $\alpha \neq \beta$, the degenerate points are opened in Fig. 3(d), and extra bandgaps are generated. Fig. 4 presents the symmetric modes of the SSM consisting of diatomic unit cells at the two degenerate points. Such band degeneracy leads to the appearance of the crossing points, and breaking the symmetry results in the opening of the degenerate points [36,40,41].

In detail, the band structure of the traditional star-shaped structure with diatomic unit cells has four branches within the specific frequency range, with its bandgap between the second and third branches ranging from 313.33 Hz to 373.06 Hz. For the proposed SSM, the original bandgap is widened, and two additional ones are generated, respectively above and below the original one. The two bandgaps range over 80.83–92.87 Hz and 484.94–551.15 Hz, respectively. These preliminary results have shown the low-frequency and broadband characteristics of the bandgaps in the proposed star-shaped truss structures. These characteristics could be advantageous for vibration reduction, particularly in scenarios where multiple low-frequency excitation sources are present.

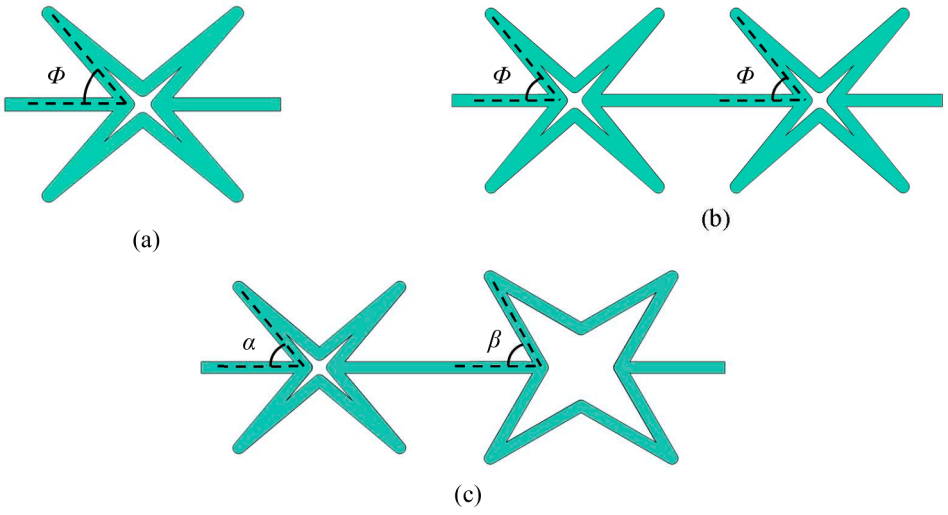

Fig. 2. Diagrams of (a) the monoatomic unit cell, (b) the enlarged (diatomic) unit cell, and (c) the diatomic unit cell of the proposed SSM.

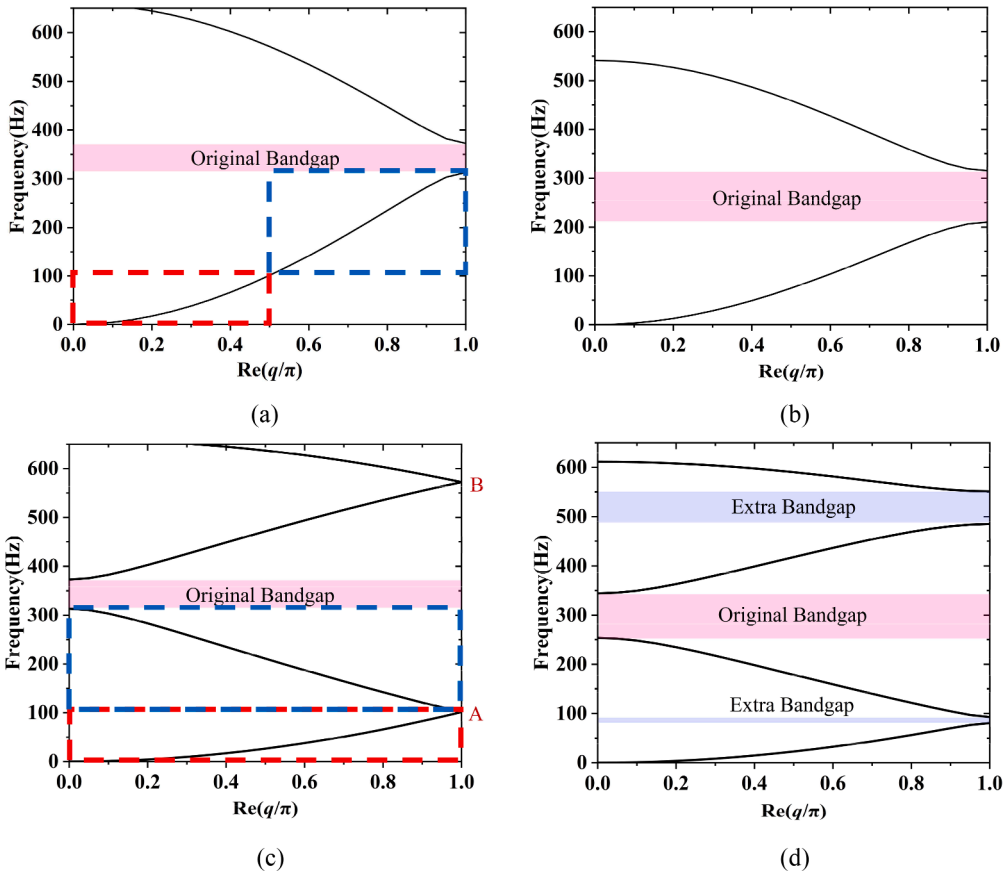

Fig. 3. Band structures of the monoatomic unit cell with (a) $\Phi = 50°$ and (b) $\Phi = 60°$, the diatomic unit cell with (c) $\Phi = 50°$ and the SSM unit cell with (d) $\alpha = 50°$ and $\beta = 60°$.

Table 1
Material and structural parameters of the SSM.

L_1 (cm)	L_2 (cm)	α (°)	β (°)	b (cm)	E (GPa)	ρ (kg/m^3)	ν
1.8	1.8	50	60	0.2	2.2e9	1100	0.394

2.3. Transmittance analysis

Furthermore, we calculated the transmittance response of the proposed SSM to verify the bandgap characteristics predicted by the band structure analysis. The sample SSM comprises eight unit cells and is modeled in the beam physical field in COMSOL, as shown in Fig. 5. Due to the non-negligible ratio of cross-section size to the length of each

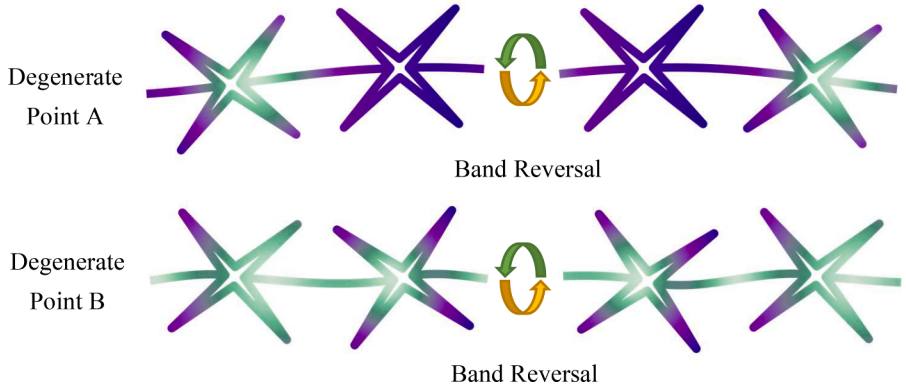

Fig. 4. Modes of the diatomic unit cell with $\Phi = 50°$ at the two degenerate points.

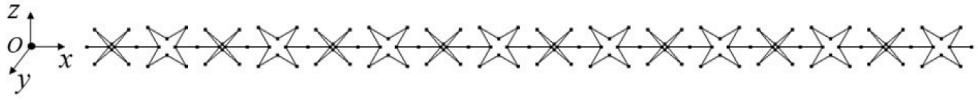

Fig. 5. The SSM model established in the beam physical field by COMSOL.

element in the proposed SSM and the presence of high-order modes in the high-frequency regime, structural shear deformation cannot be neglected. Hence, the struts are modeled as Timoshenko beam elements. The external harmonic excitation is applied on the left side of the SSM in the z-direction. The displacement response at the right end is detected during frequency sweeping. Transmittance Γ_{SSM} is defined as [42]

$$\Gamma_{SSM} = 20 \times log_{10}\frac{d_{Free}}{d_{Clamped}}, \tag{2}$$

where d_{Free} and $d_{Clamped}$ are, respectively, the displacements of the free and clamped ends in the transverse direction.

Fig. 6 illustrates the frequency response of the SSM over the frequency range from 0 to 450 Hz. It is worth noting that the transmittance curve exhibits three troughs, which correspond to the frequency ranges of 68–81 Hz, 214–274 Hz, and 406–430 Hz, respectively. These bandgaps align with the ones identified in the previous band structure analysis. However, there are errors in the width prediction. It is important to remember that the unit cell of the SSM was modeled using a solid physical field to calculate the dispersion relation in the previous section. Consequently, the discrepancy can be attributed to the utilization of different physical fields for the band structure and transmittance analyses. Despite this disparity, both models demonstrate the occurrence of band folding and opening phenomena.

3. Spectral element modeling

Though the finite element method is versatile, its computational efficiency is relatively low, especially when one wants to extend the study into high-frequency ranges, and the mesh model needs to be refined to ensure convergence. Considering the SSM is constituted of beam and rod elements, the spectral element method is very suitable for modeling such simple structures with extremely high efficiency. In this section, a dynamic model of the SSM structure is established using the SEM, and the vibration transmittance is calculated and compared with the FEM results. Typically, the SEM models structural dynamics using a concept similar to the FEM based on assembling dynamic stiffness matrices. Unlike the FEM, the SEM considers the wave solution as an interpolation function dependent on the frequency [43]. When modeling the SSM structures, we primarily consider their axial and transverse deformations.

The partial differential motion equation of the axially vibrating rod is described by [23]

$$EA\frac{\partial^2 u(x,t)}{\partial x^2} - \rho A\frac{\partial^2 u(x,t)}{\partial t^2} = 0, \tag{3}$$

where the axial displacement is defined as $u(x, t)$, E represents Young's modulus, and ρ is the mass density of the rod. The general solution to Eq. (3) can be assumed by

$$u(x,t) = \frac{1}{N}\sum_{n=0}^{N-1} U_{Rn}(x,\omega_n)e^{i\omega_n t}, \tag{4}$$

where $U_{Rn}(x, \omega_n)$ is the spectral component of the axial displacement, ω_n represents the circular frequency. By substituting Eq. (4) into Eq. (3), one converts the governing equation into the frequency domain.

$$EA\frac{\partial^2 U_{Rn}}{\partial x^2} + \omega^2\rho A U_{Rn} = 0. \tag{5}$$

The general solution can be written as

$$U_{Rn}(x,\omega_n) = B_1 e^{-ik_L x} + B_2 e^{ik_L x}, \tag{6}$$

where $k_L = \omega\sqrt{\rho/E}$, B_1 and B_2 are the coefficients that are determined by the node displacement of the rod. U_{R1} and U_{R2} are used to represent the node displacements of the rod, which can be written as

$$d_R = [\,U_{R1} \quad U_{R2}\,]^T = [\,U_R(0) \quad U_R(L)\,]^T. \tag{7}$$

One can obtain

$$U_{Rn}(x) = N_{R1}U_{R1} + N_{R2}U_{R2}, \tag{8}$$

where $N_{R1}(x, \omega) = \csc(k_L L)\sin(k_L(L-x))$ and $N_{R2}(x, \omega) = \csc(k_L L)\sin(k_L x)$ are the frequency-dependent shape functions.

The axial force can be derived by the spectral representation [23]

$$f(x,t) = \frac{1}{N}\sum_{n=0}^{N-1} H(x,\omega_n)e^{i\omega_n t}. \tag{9}$$

The relationship between the displacement and force in the frequency domain can be described as

$$H(x,\omega_n) = EA\frac{\partial U_{Rn}(x,\omega_n)}{\partial x}. \tag{10}$$

The nodal forces at the two ends of the rod element can be expressed in matrix form as

$$f_c(\omega) = [\,N_{R1} \quad N_{R2}\,]^T = [\,N_R(0) \quad N_R(L)\,]^T. \tag{11}$$

Therefore, one obtains

$$S_R(\omega)d_R = f_c(\omega), \tag{12}$$

where $\mathbf{S}_R(\omega)$ is the dynamic stiffness matrix of the rod element and can be written as

$$S_R(\omega) = \frac{EAk_L}{\sin(k_L L)}\begin{bmatrix}\cos(k_L L) & -1\\ -1 & \cos(k_L L)\end{bmatrix}. \tag{13}$$

The corresponding dynamic stiffness matrix of the beam element can also be derived by following similar procedures [23]. Usually, when the ratio of the beam's cross-section size to its length is not extremely small, shear deformation becomes a significant factor to consider, and the Timoshenko beam theory needs to be used.

The partial differential vibration equation of the Timoshenko beam element is described by

$$\kappa AG\left(\frac{\partial\theta_B(x,t)}{\partial x} - \frac{\partial^2 w_B(x,t)}{\partial x^2}\right) = \rho A\frac{\partial^2 w_B((x,t)}{\partial t^2}, \tag{14}$$

$$EI\frac{\partial^2\theta_B(x,t)}{\partial x^2} + \kappa GA\left(\frac{\partial w_B(x,t)}{\partial x} - \theta_B(x,t)\right) - \rho I\frac{\partial^2\theta_B(x,t)}{\partial t^2} = 0, \tag{15}$$

where κ is related to the cross-section shape, G represents the shear modulus, A represents the cross-section area, I is the area moment of inertia of the beam cross-section, w_B represents the transverse displacement, θ_B represents the rotational angle of the beam cross-section. The transverse displacement and rotation angle of a

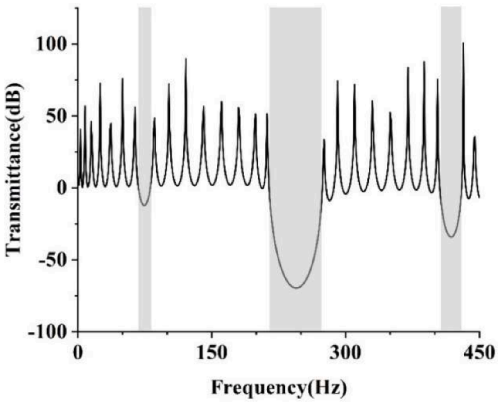

Fig. 6. The transmittance of the SSM containing 8 unit cells.

Timoshenko beam are given as follows:

$$w_B(x,t) = \frac{1}{N}\sum_{n=0}^{N-1} W_n(x,\omega_n)e^{i\omega_n t}, \tag{16}$$

$$\theta_B(x,t) = \frac{1}{N}\sum_{n=0}^{N-1} \Theta_n(x,\omega_n)e^{i\omega_n t}. \tag{17}$$

Substituting Eqs. (16)–(17) into Eqs. (14)–(15), the governing equations are transformed into

$$\kappa GA\left(\frac{\partial^2 W_n}{\partial x^2} - \frac{\partial \Theta_n}{\partial x}\right) + \rho A {W_n}{\omega_n}^2 = 0, \tag{18}$$

$$EI\frac{\partial^2 \Theta_n}{\partial x^2} + \kappa GA\left(\frac{\partial W_n}{\partial x} - \Theta_n\right) + \rho I \Theta_n {\omega_n}^2 = 0. \tag{19}$$

The general solutions to Eqs. (18)–(19) are assumed to be

$$W_n(x) = Re^{-ikx}, \tag{20}$$

$$\Theta_n(x) = \gamma Re^{-ikx}, \tag{21}$$

where R and γ are to-be-determined coefficients depending on ω.

The characteristic equation can be obtained by inserting Eqs. (20)–(21) into Eqs. (18)–(19):

$$k^4 - \eta k_F^4 k^2 - k_F^4\left(1 - \frac{\rho I}{\kappa GA}\omega^2\right) = 0. \tag{22}$$

One can obtain four roots by solving Eq. (22) as follows:

$$k_1 = -k_2 = \frac{k_F}{\sqrt{2}}\sqrt{\eta k_F^2 + \sqrt{\eta^2 k_F^4 + 4\left(1 - \frac{\rho I}{\kappa GA}\omega^2\right)}} = k_t, \tag{23}$$

$$k_3 = -k_4 = \frac{k_F}{\sqrt{2}}\sqrt{\eta k_F^2 - \sqrt{\eta^2 k_F^4 + 4\left(1 - \frac{\rho I}{\kappa GA}\omega^2\right)}} = k_e, \tag{24}$$

where $\mathrm{k_F} = \sqrt{\omega}\left(\frac{\rho}{\mathrm{E}}\right)^{\frac{1}{4}}$, $\eta = \frac{\mathrm{I}}{\mathrm{A}} + \frac{\mathrm{EI}}{\kappa \mathrm{GA}}$. Moreover, the coefficient γ is deduced as

$$\gamma_q(\omega) = \frac{1}{ik_q}\left(k_q^2 - \frac{\rho}{\kappa G}\omega^2\right), (q = 1,2,3,4). \tag{25}$$

Thus, the general solutions to Eqs. (18)–(19) can be derived as the following form

$$W_n(x,\omega) = R_1 e^{-ik_t x} + R_2 e^{ik_t x} + R_3 e^{-ik_e x} + R_4 e^{ik_e x}, \tag{26}$$

$$\Theta_n(x,\omega) = \gamma_1 R_1 e^{-ik_t x} + \gamma_2 R_2 e^{ik_t x} + \gamma_3 R_3 e^{-ik_e x} + \gamma_4 R_4 e^{ik_e x}. \tag{27}$$

The node displacement and rotation angle of the two ends of the beam are written as

$$d_B = \begin{bmatrix} W_1 \\ \Theta_1 \\ W_2 \\ \Theta_2 \end{bmatrix} = \begin{bmatrix} W(0) \\ \Theta(0) \\ W(L) \\ \Theta(L) \end{bmatrix}. \tag{28}$$

The shear and bending moments are expressed as follows:

$$Q = \kappa GA\left(\frac{\partial W}{\partial x} - \Theta\right), \tag{29}$$

$$M = EI\frac{\partial \Theta}{\partial x}. \tag{30}$$

The node force of the beam can be written as

$$f_B = \begin{bmatrix} Q_1 \\ M_1 \\ Q_2 \\ M_2 \end{bmatrix} = \begin{bmatrix} -Q(0) \\ -M(0) \\ Q(L) \\ M(L) \end{bmatrix}. \tag{31}$$

Then, the relationship between the node displacement and the nodal force is given by

$$S_B(\omega)d_B = f_B, \tag{32}$$

where $\mathbf{S}_B(\omega)$ is the dynamic stiffness matrix of a Timoshenko beam element.

By using the finite element assembly concept, the stiffness matrices of the beam and rod elements can be assembled to obtain the overall stiffness matrix of the SSM in the global coordinate system. Subsequently, the relationship between the node displacement and the node force of SSM can be obtained as

$$F = S_{SSM}(\omega)U, \tag{33}$$

where $\mathbf{S}_{SSM}(\omega)$ is the global dynamic stiffness matrix of the SSM; **F** and **U** are the nodal force and displacement, respectively. By solving Eq. (33), the structural dynamic responses can be calculated.

4. Experimental validation

The SSM prototype designed in this work consists of a periodic array of unit cells along the x-axis, as shown in Fig. 2(c). The physical prototype was 3D printed using Polylactic acid (PLA) material. The specific material and structural parameters are listed in Table 1. The sample prototype was designed with 6 unit cells to guarantee a strong periodicity, making the bandgap easily detectable. Previous studies indicated that a minimum of 5~6 unit cells suffices to guarantee periodicity [44]. The decrease in the number of unit cells weakens the vibration suppression ability but does not significantly influence the bandgap position [45]. Due to the complexity of the SSM structure and the relative fragility of PLA materials, fixtures are used to clamp both ends of the structure to prevent large deformation caused by gravity or bolt preload. The experimental setup, including a computer, an accelerometer, a shaker, a power amplifier, and a multi-channel data acquisition system, is shown in Fig. 7. During the test, the shaker generates an excitation, sweeping from 5 Hz to 450 Hz, to the right end of the SSM prototype. The accelerometer installed on the left side measures the output response.

The frequency responses of the SSM structure, determined using numerical simulation, theoretical modeling, and experimental test, are compared in Fig. 8. It is clear from Fig. 8(a) that the results obtained using the SEM and FEM approaches are almost identical since both are modeled using the Timoshenko beam theory. The experimental result is shown in Fig. 8(b). There are three distinct troughs in the frequency range of 0–450 Hz, corresponding to the three bandgaps. Overall, the experimental result matches well with the theoretical prediction despite the abscissa unit in Fig. 8(b) being different from that in Fig. 8(a).

The main reasons for the errors between the experimental and theoretical results of the SSM structure are encapsulated as

(a) Initial structural deformation existed even when both ends were fixed. PLA materials are relatively soft, and due to the small cross-section, the slender structure is too fragile to maintain a horizontal posture, i.e., slight static deformation occurred due to the gravity effect, resulting in an inevitable error.
(b) Extending the structural periodicity enhances the vibration suppression effect, i.e., deepening the trough of the corresponding bandgap in the frequency response curve. However, the fixture size and experimental conditions limited the number of cells in the manufactured physical prototype, thus weakening the bandgap effect detected in the experiment.

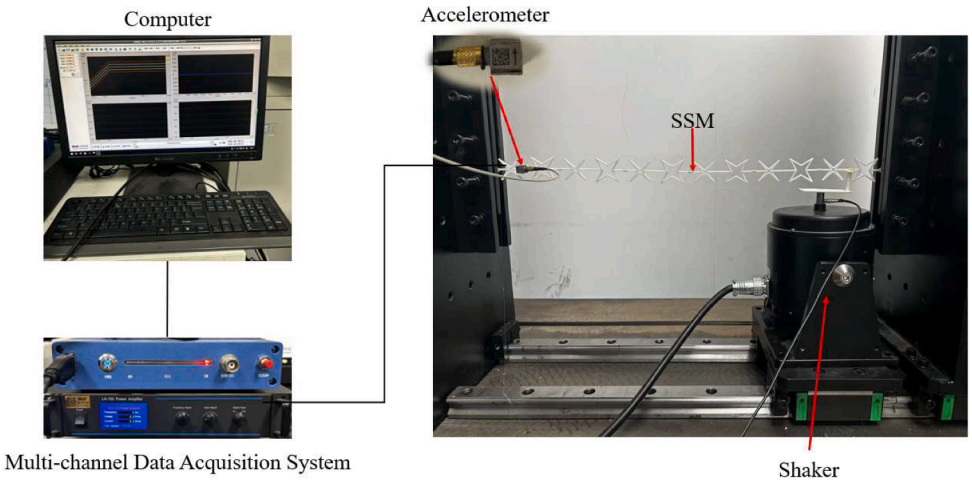

Fig. 7. The complete experiment setup and the physical prototype.

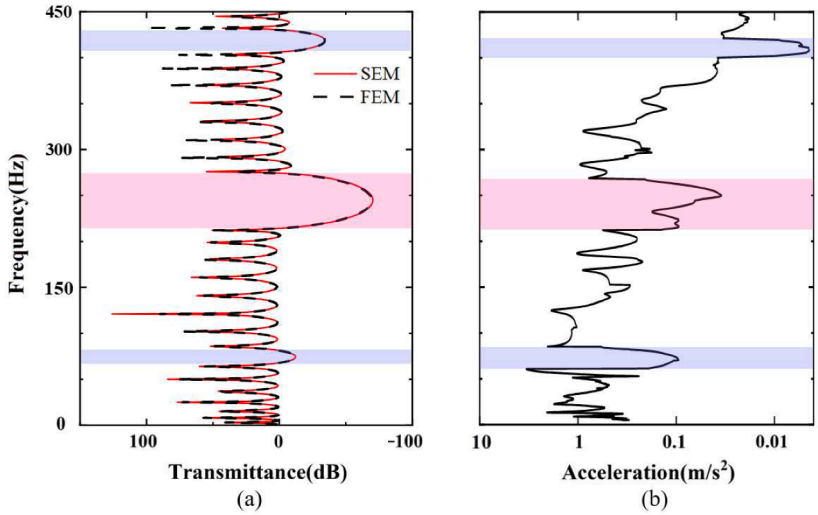

Fig. 8. Frequency response curves of the SSM consisting of 8 unit cells obtained by (a) SEM, FEM, and (b) experiment.

(c) Given the experimental conditions, factors such as the weight of the accelerometer and the stress on the wires likely influenced the vibration test to some extent. Therefore, the dynamics of the physical prototype cannot fully match the experimental one.

5. Structural parametric study

The geometry of an SSM is shaped by a few crucial structural parameters, including the strut length L_2, the concave angles α and β between the horizontal strut and the inclined one, and the strut's cross-section area A. Changing these parameters will affect the mechanical and dynamic properties of an SSM, as well as the degenerate point opening phenomenon in the band structure. Thus, by adjusting these parameters individually, we delve into studying how they affect the bandgaps regarding the width, position, and number. The SSM under investigation in this section consists of 8 unit cells, and the parametric study results are presented below.

5.1. Effect of concave angle

The SSM representative volume element (RVE) designed in this paper comprises two star-shaped substructures with different concave angles to open the degenerate points and produce more bandgaps. Therefore, the concave angle is the key factor that breaks the spatial symmetry of the structure. As a periodic structure, the SSM with $\alpha = 50^\circ$ and $\beta = 60^\circ$ has identical bandgaps as that with $\alpha = 60^\circ$ and $\beta = 50^\circ$ To analyze the effect of concave angles on the bandgap properties of SSM structures, it is sufficient to select either α or β for examination. In our study, we remained α of the first substructure constant and varied β of the second substructure.

Fig. 9 displays the variation trend of the bandgaps of the SSM identified in transmittances when $\alpha = 50^\circ$ and β progressively varies. Over the frequency range of 0–450 Hz, there is just one bandgap when β is identical to α, i.e., $\beta = 50^\circ$ No extra bandgaps are formed in this configuration since the SSM with $\beta = 50^\circ$ still follows a conventional design without the degenerate point opening phenomena. As β increases and becomes different from α, two extra bandgaps (labeled I and III) are produced below and above the original bandgap (labeled II) due to the degenerate point opening phenomenon. Moreover, the original bandgap II slightly moves toward the lower frequency region, getting broader and deeper.

In addition, the bandgaps I and III also expand and shift toward lower frequency zones as β increases. These results differ from the bandgap characteristics of common periodic structures whose bandgaps usually get narrowed when shifting to the lower frequency zones [46]. Obviously, this phenomenon renders the proposed SSM more suitable for low-frequency broadband vibration suppression. It is worth noting that when $\beta = 55^\circ$, the two troughs corresponding to bandgaps I and III are

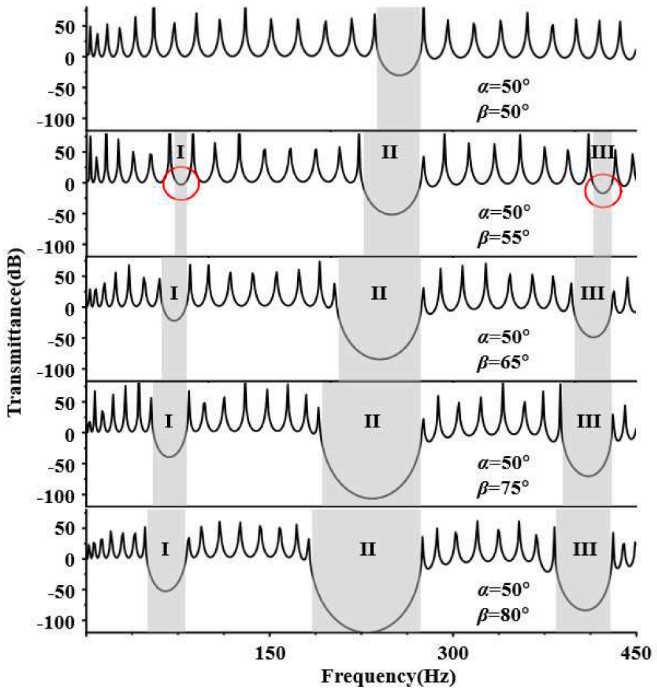

Fig. 9. The transmittance of the SSM with $\alpha = 50°$ and various β.

not noticeably apparent, which means that if the difference in concave angles between the two star-shaped substructures is small, the vibration suppression abilities of the two extra bandgaps are very limited.

Overall, the vibration suppression performance of SSM is worst when the difference in concave angles between two substructures is the smallest ($\alpha = 50°$ and $\beta = 55°$). Conversely, the greatest vibration suppression effect is achieved when the difference in concave angles between the two substructures is the largest ($\alpha = 50°$ and $\beta = 85°$). The bandgaps of the proposed SSM steadily move towards the low-frequency region and get broader as the difference in concave angles rises.

5.2. Effect of strut length

As previously indicated, the degenerate points were opened by setting two distinct concave angles of the neighboring substructures, which were crucial for the formation of extra bandgaps in the SSM. If the lengths of the struts in the two substructures of the RVE are different, we speculate that structural asymmetry can also be achieved, and extra bandgaps can also form. In order to investigate this feasibility, we analyze an SSM with $\alpha = \beta = 50°$ but having different L_1 and L_2 in this section. In particular, we set $L_1 = 1.8$ cm in the first substructure and $L_2 = 1.9$ cm in the second substructure. It is found that only one extra bandgap appears below 450 Hz, as shown in Fig. 10. Interestingly, this phenomenon is different from those with different concave angles in the previous section. This is because, compared to the strut length, the concave angle is a more vital characteristic parameter of star-shaped truss structures, having a more substantial impact on spatial symmetry. Still, the varied strut lengths in the two neighboring substructures changed the symmetry to a small extent. Thus, one extra bandgap is produced.

In order to further analyze the effect of strut length on the bandgaps of the SSM, we continously varied L_2 from 1.6 cm to 2.0 cm. The transmittance contour, as shown in Fig. 11, reveals how the bandgaps of the SSM change as L_2 increases. It is shown that the first bandgap moves towards lower frequencies as L_2 grows while its width remains relatively constant. This characteristic indicates the adjustability of the bandgap position. As for the second bandgap, it first narrows till it disappears, then re-emerges and gradually widens. This process refers to the closing

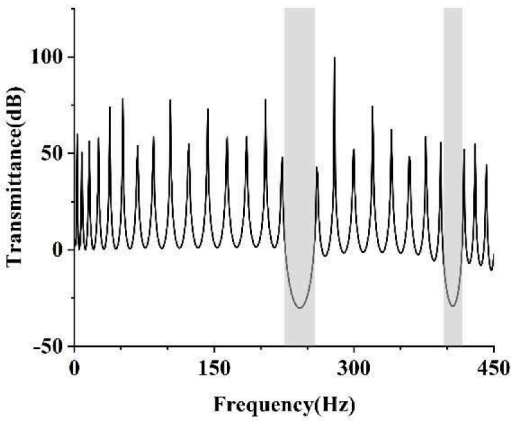

Fig. 10. The transmittance of the SSM with $L_1 = 1.8$ cm and $L_2 = 1.9$ cm.

and re-opening phenomena of the degenerate points. The second bandgap gets broader as the difference between L_1 and L_2 becomes greater. Moreover, as shown in Fig. 11, a deeper transmittance trough marked in red indicates a stronger vibration suppression effect. Due to the geometric relationship $a = L_1 \times [1\text{-}\cos(\alpha)+\sin(\alpha)] + L_2 \times [1\text{-}\cos(\beta)+\sin(\beta)]$, an increase in L_2 actually causes the periodic SSM structure's lattice constant to rise, which provides an explanation for the widening of the bandgap.

5.3. Effect of strut cross-section

This section investigates the influence of the cross-section area A of the strut. We intentionally alter the cross-section areas of the two star-shaped substructures within the RVE to break the structural symmetry. In that case, significant mutations may occur in the connection zones of the struts, which can then easily lead to the deformation of the connection positions. Therefore, in this section, the cross-section area A of all substructures changes synchronously to maintain structural continuity, while other parameters are kept the same as those in Table 1, to explore the impact of changes in the cross-section areas of the struts on the bandgap characteristics of the SSM. Because the SSM is a truss structure composed of slender strut elements, any changes in the slender struts alter the dynamics. The adjustment parameter in this section is the cross-section side length b of the square cross-section strut, and the calculation results are presented in Fig. 12. It can be observed that all of the three bandgaps move toward high-frequency zones as b increases. The second bandgap slightly gets widened, while the widths of the first and third bandgaps remain almost unchanged. Overall, the locations of the bandgaps have a positive correlation with the cross-section size, and it is noteworthy to consider the parameters used in the context of lightweight application backgrounds.

5.4. Effect of folding order

Previous studies showed that two extra bandgaps are produced in the band structure of the SSM with an RVE having two different star-shaped substructures, e.g., varied concave angles. Hereinafter, we refer to the number of star-shaped substructures in an RVE as the folding order. According to this definition, one knows that the folding orders of the SSM structures studied in previous sections are two. Similar to the concept of synergetic coupling to increase mode distribution density for finally achieving broadband vibration suppression [47–49], we can speculate that more bandgaps will be generated if we construct the SSM having an RVE with multiple different star-shaped substructures, i.e., increase the folding order. To investigate the impact of the folding order on the vibration suppression performance of such truss structures, we designed SSM structures with third-folding and fourth-folding orders, as shown in Fig. 13, in which the numbers of different concave angles in a

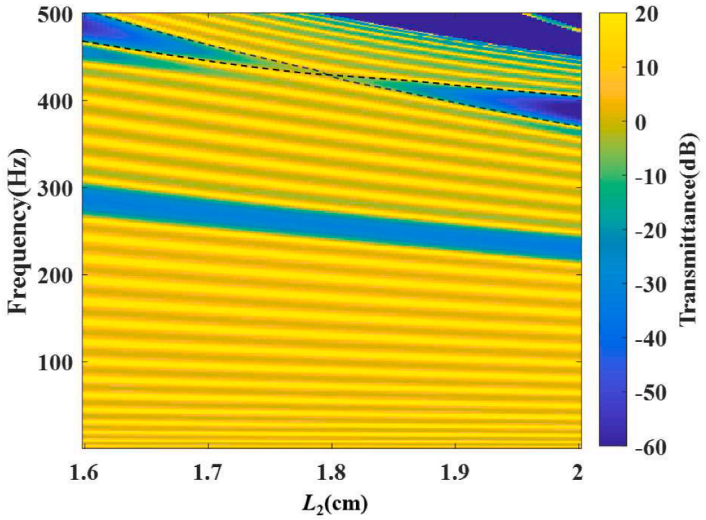

Fig. 11. Effect of L_2 on bandgaps of the SSM.

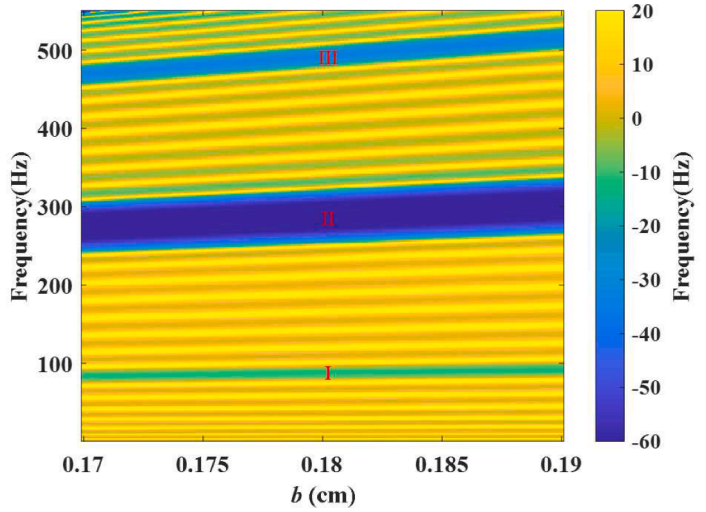

Fig. 12. Effect of b on bandgaps of the SSM.

single SSM RVE are three and four, respectively. According to the band folding mechanism, increasing the number of unit cells in an RVE to three and four times will cause each band to fold twice and thrice, respectively. Each folding will produce a point, and a corresponding extra bandgap will appear due to the destruction of spatial symmetry. Since those bandgaps are not independently generated, they cannot be easily adjusted in a completely separate manner.

We calculated the vibration transmittances of these high-order SSM

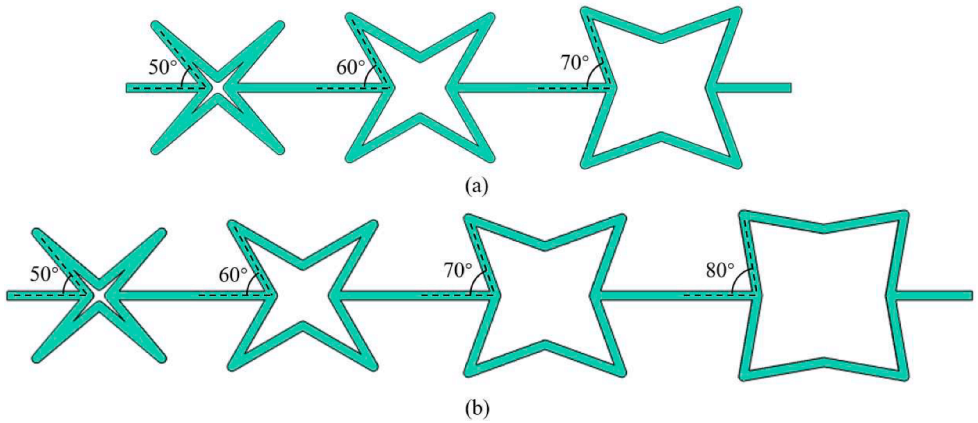

Fig. 13. The RVE of the (a) third and (b) fourth-order band folded SSMs.

structures rather than band structures because previous research revealed that the increase of folding order may affect the depths of bandgap troughs, and transmittance plots can more easily capture these features [46]. The proposed SSM structures with third- and fourth-order folding are composed of eight RVEs, with one end fixed and the other free. The transmittance results of the two proposed SSM structures are presented in Fig. 14, from which it is noted that more degenerate points are opened with the increase of the folding order, leading to more bandgaps within the frequency range of 0–450 Hz. Better vibration suppression performance is also indicated by the bandgaps shifting toward the low-frequency region and main bandgap troughs deepening. This phenomenon is beneficial to suppressing multiple vibration waves with spanned frequencies, which can be utilized to filter multiple signals in practice. It is also worth mentioning that several troughs corresponding to the extra bandgaps caused by the band folding effect are pretty shallow. This indicates that the vibration suppression abilities of some bandgaps are relatively poor, a limitation attributed to the constraints of the band folding design strategy.

6. Further discussion

This work demonstrates that the band folding mechanism can be introduced in star-shaped metamaterials to produce more low-frequency bandgaps for broadband vibration suppression. The band folding design strategy is generic and can be employed and extended to other designs, such as metamaterials with acoustic black holes (ABHs) [28,47] and other multi-mode bandgap construction methods [50]. Moreover, though the design presented in this study is a 1D structure, it can be speculated that if one extends the design by well configuring a 2D pattern, a 2D SSM with broadband vibration suppression abilities in two directions will be achieved.

The following presents a simple 2D example. Fig. 15 demonstrates the unit cell of a 2D star-shaped structure. The concave angle is $\Phi = 70^{\circ}$, and the square-sectioned strut's side length is 2 mm. Assuming the 2D pattern extends to infinity in both horizontal and vertical directions, Fig. 16(a) depicts the first Brillouin zone, and Fig. 16(b) shows the corresponding band structure. Due to the symmetry of the square unit cell, the analysis can be confined to the irreducible Brillouin zone (IBZ) in the shadow area. Moreover, since extremums are always on the zone boundary, one only needs to search along the boundary of the IBZ. As observed in Fig. 16(b), there is only one full band gap ranging over 1012–1233 Hz. It implies that the effective vibration suppression bandwidth is about 221 Hz below 1500 Hz.

Following the band folding strategy, we first consider an intentionally enlarged unit cell, as shown in Fig. 17(a). The enlarged unit cell contains four unit cells from Fig. 15 with identical parameters. Fig. 18(a) shows the corresponding band structure of the enlarged unit cell. It can be noted that more bands appear, and crossing points are found at the

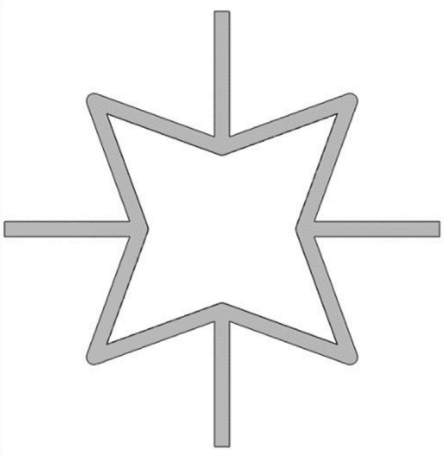

Fig. 15. Monoatomic unit cell of a 2D star-shaped metamaterial.

corner points of the IBZ, i.e., **X** and **M**. The crossing points are formed by the band folding mechanism we used in previous sections for the 1D SSM. However, there is still only one bandgap spanning the same frequency range from 1012 Hz to 1233 Hz below 1500 Hz.

We then convert the fake primitive unit cell shown in Fig. 17(a) into an authentic one, as shown in Fig. 17(b), by changing the strut's side length of the two "atoms" at the anti-diagonal from 2 mm to 1.5 mm. This is the scheme we utilized in Section 5.3 for the 1D SSM. Fig. 18(b) presents the band structure of the newly obtained 2D SSM. Compared with Fig. 18(a), one observes that two more bandgaps appear below 1500 Hz, with one below and the other above the original bandgap. By carefully inspecting the curve patterns at the IBZ corners (**X** and **M**), one can find that some crossing points are opened, which leads to the formation of the two new full bandgaps. Those three bandgaps, respectively, range over 408–437 Hz, 810–1136 Hz, and 1234–1387 Hz. Summing the three up yields a 508 Hz bandwidth for vibration suppression, representing a 129.8 % improvement compared to the traditional one (Fig. 15 and Fig. 17(a)) without adopting the band folding mechanism. The transmittance analysis of the 2D SSM is not presented for redundancy, as it is well-known and can be found in numerous literatures that band structure analysis can well predict the transmittance response. The band structure analysis gives us confidence that this newly developed 2D SSM can achieve broadband vibration suppression. The other schemes in Section 5 can also be used to develop this 2D SSM, producing additional bandgaps for broadband vibration suppression.

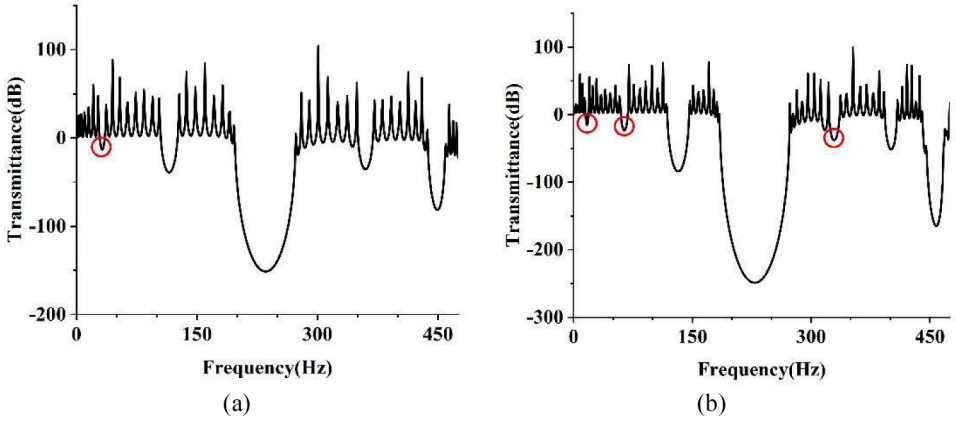

Fig. 14. The transmittances of the (a) third-order and (b) fourth-order SSMs.

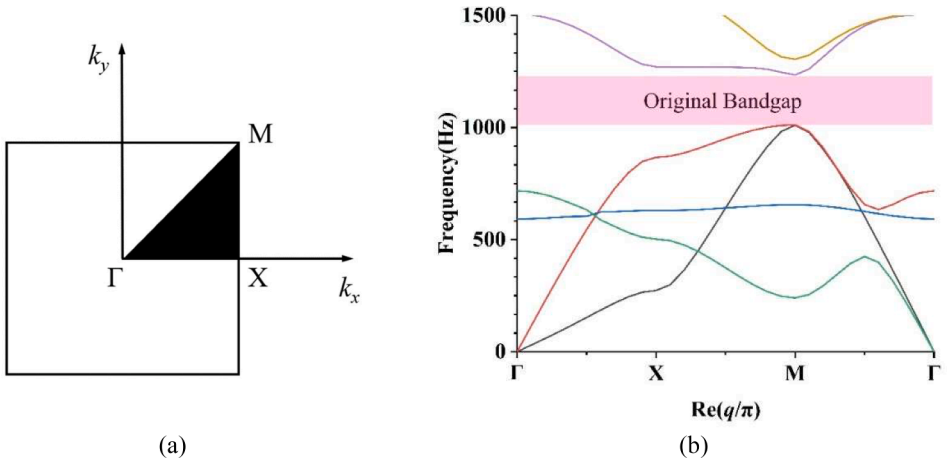

Fig. 16. (a) The first Brillouin zone and the irreducible Brillouin zone (shadow area); and (b) band structure of the 2D star-shaped metamaterial.

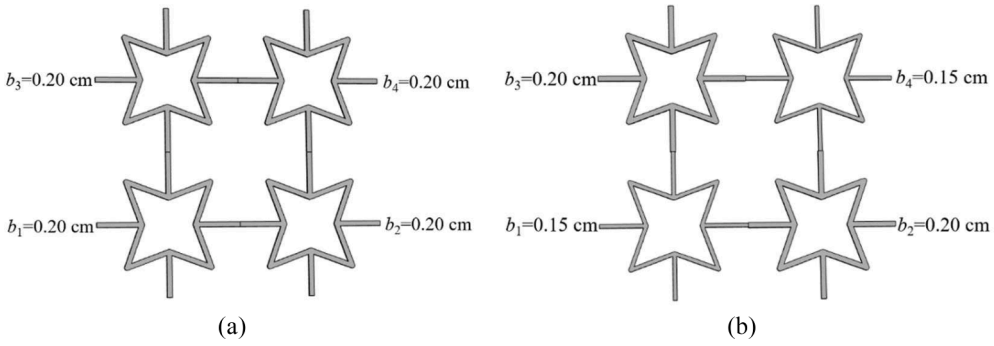

Fig. 17. (a) Enlarged unit cell with the same parameters as in Fig. 15, (b) four-atomic unit cell with the anti-diagonal being modified.

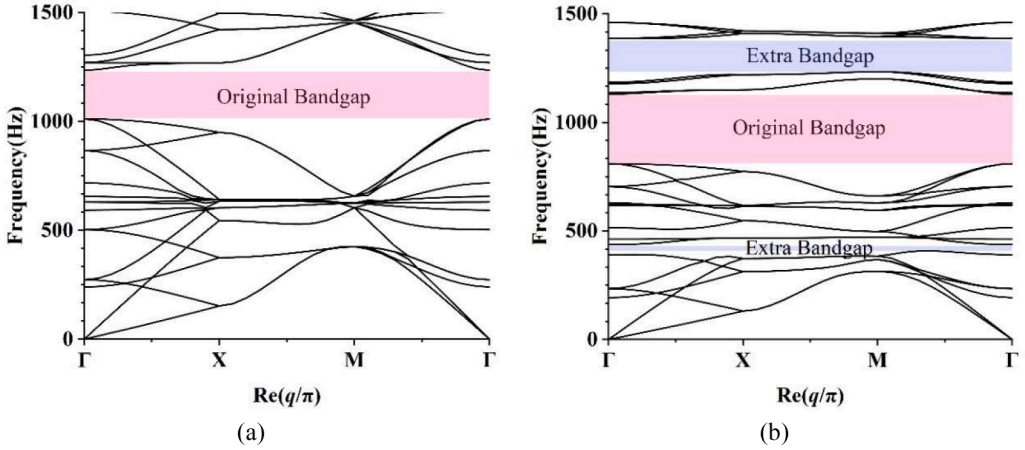

Fig. 18. (a) Band structure of the enlarged unit cell, (b) band structure of the four-atomic unit cell with the anti-diagonal being modified.

7. Conclusion

This study has proposed and presented an SSM with low-frequency and broadband vibration suppression abilities. A diatomic unit cell is constructed based on the band folding mechanism, and the concave angle of one of the unit cells is changed as a geometric parameter to break spatial symmetry. The degenerate points are then opened to achieve multiple bandgaps for the SSM in the low-frequency range. An FE model has been built to investigate the bandgap characteristics of the proposed SSM. A theoretical model has also been established using the SEM. The FEM, SEM, and experimental results were compared for mutual validation. The effects of different structural parameters, including the strut length L_2, concave angles β, and cross-section area A on the transmittance of the SSM, were analyzed. In addition, we further proposed the concept of high-order SSMs, and the effect of the folding order on the bandgaps of the SSM was also investigated. The key conclusions from the analyses are summarized as follows:

- By breaking the spatial symmetry, the proposed SSM structure can produce extra bandgaps by opening degenerate points in the band structure.

- FEM simulations, SEM calculations, and experimental tests have all been conducted to validate the formation of multiple bandgaps in the proposed SSM.
- With the increase of the difference in concave angles between two substructures in each SSM RVE, the bandgaps of the SSM will get wider and move to the low-frequency zone. In addition, all the bandgaps of the SSM move to the high-frequency direction as the cross-section area A increases.
- Suppose the concave angles of the two star-shaped substructures in an RVE are the same while the lengths of the struts are different. In this case, with a slight increase of L_2, the SSM structure may only open one extra bandgap.
- According to the high-order band folding strategy, as the folding order increases, the SSM can open up more degenerate points and, thus, generate more bandgaps.

Furthermore, a 2D star-shaped metamaterial design based on the band folding strategy is showcased to extend the applications. By following a similar design scheme, the 2D SSM has also been found to produce extra bandgaps, which underscores the innovation and applicability of the approach presented in this paper.

In general, this work has presented a design strategy for periodic star-shaped truss structures to produce multiple bandgaps in the low-frequency range, which is beneficial for broadband vibration isolation and filtering applications. This concept based on the band folding mechanism can be universally implemented in designing other periodic structures, with careful attention given to accommodating different stiffness and bearing capacity requirements.

CRediT authorship contribution statement

Zhenkun Guo: Writing – original draft, Validation, Methodology, Investigation, Funding acquisition, Formal analysis, Conceptualization. **Jiaqi Wen:** Writing – original draft, Validation, Software, Methodology, Investigation, Formal analysis, Data curation. **Yongjun Shen:** Writing – review & editing, Supervision, Project administration, Formal analysis. **Guobiao Hu:** Writing – review & editing, Supervision, Investigation, Funding acquisition, Formal analysis, Conceptualization. **Guoqing Jiang:** Writing – review & editing, Resources, Project administration, Formal analysis.

Declaration of competing interest

The authors declare that they have no known competing financial interests or personal relationships that could have appeared to influence the work reported in this paper.

Data availability

Data will be made available on request.

Acknowledgments

This study is financially supported by the National Natural Science Foundation of China (No. 12102031, 52305135), the Pyramid Talent Training Project of Beijing University of Civil Engineering and Architecture (No. JDYC20220828), S&T Program of Hebei (No. 215676145H), the Guangdong Provincial Key Lab of Integrated Communication, Sensing and Computation for Ubiquitous Internet of Things (No. 2023B1212010007), the Hong Kong University of Science and Technology (Guangzhou), and Guangzhou Municipal Bureau of Science and Technology (SL2023A04J01741, SL2023A03J00869).

References

[1] M.I. Hussein, M.J. Leamy, M. Ruzzene, Dynamics of phononic materials and structures: historical origins, recent progress, and future outlook, Appl. Mech. Rev. 66 (4) (2014) 040802.
[2] Muhammad, C. Lim, From photonic crystals to seismic metamaterials: a review via phononic crystals and acoustic metamaterials, Arch. Comput. Methods Eng. 29 (2) (2022) 1137–1198.
[3] M.H. Bae, J.H. Oh, Nonlinear elastic metamaterial for tunable bandgap at quasi-static frequency, Mech. Syst. Signal Process. 170 (2022) 108832.
[4] Z. Guo, G. Hu, J. Jiang, L. Yu, X. Li, J. Liang, Theoretical and experimental study of the vibration dynamics of a 3D-printed sandwich beam with an hourglass lattice truss core, Front. Mech. Eng. 7 (2021) 651998.
[5] Y. Zhang, Z. Li, K. Xu, J. Zang, A lattice sandwich structure with the active variable stiffness device under aerodynamical condition, Aerosp. Sci. Technol. 116 (2021) 106849.
[6] J. Redondo, L. Godinho, K. Staliunas, J.V. Sánchez-Pérez, An equivalent lattice-modified model of interfering Bragg bandgaps and Locally Resonant Stop Bands for phononic crystal made from Locally Resonant elements, Appl. Acoust. 211 (2023) 109555.
[7] J. Guo, Y. Li, Y. Xiao, Y. Fan, D. Yu, J. Wen, Multiscale modeling and design of lattice truss core sandwich metastructures for broadband low-frequency vibration reduction, Compos. Struct. 289 (2022) 115463.
[8] Y. Xue, J. Li, Y. Wang, F. Li, Tunable nonlinear band gaps in a sandwich-like meta-plate, Nonlinear Dyn. 106 (2021) 2841–2857.
[9] X. Fang, J. Wen, B. Bonello, J. Yin, D. Yu, Ultra-low and ultra-broad-band nonlinear acoustic metamaterials, Nat. Commun. 8 (1) (2017) 1288.
[10] C. Cai, J. Zhou, K. Wang, Q. Lin, D. Xu, G. Wen, Quasi-zero-stiffness metamaterial pipe for low-frequency wave attenuation, Eng. Struct. 279 (2023) 115580.
[11] Y. Xue, J. Li, Y. Wang, Z. Song, A.O. Krushynska, Widely tunable magnetorheological metamaterials with nonlinear amplification mechanism, Int. J. Mech. Sci. (2023).
[12] J. Li, Y. Xue, F. Li, Active band gap control of magnetorheological meta-plate using frequency feedback control law, J. Sound Vib. 567 (2023) 118076.
[13] W. Tian, T. Zhao, Z. Yang, Supersonic meta-plate with tunable-stiffness nonlinear oscillators for nonlinear flutter suppression, Int. J. Mech. Sci. 229 (2022) 107533.
[14] W. Tian, T. Zhao, Z. Yang, Theoretical modelling and design of metamaterial stiffened plate for vibration suppression and supersonic flutter, Compos. Struct. 282 (2022) 115010.
[15] T. Zhao, Z. Yang, W. Tian, Tunable nonlinear metastructure with periodic bi-linear oscillators for broadband vibration suppression, Thin-Walled Struct. 191 (2023) 110975.
[16] L. Xiao, O.S. Bursi, M. Wang, S. Nagarajaiah, F. Sun, X.-L. Du, Metamaterial beams with negative stiffness absorbers and rotation: band-gap behavior and band-gap merging, Eng. Struct. 280 (2023) 115702.
[17] L. Xiao, M. Iqbal, X. Yu, Quasi-static band gaps in metamaterial pipes with negative stiffness resonators, Int. J. Mech. Sci. 261 (2024) 108668.
[18] W. Dong, T. Wang, Z. Huang, M. Chen, Q. Li, W. Jia, Characteristics of band gaps of a metamaterial plate with membrane-type resonators based on the energy approach, Thin-Walled Struct. 191 (2023) 110930.
[19] M. Zhang, J. Yang, R. Zhu, Origami-based bistable metastructures for low-frequency vibration control, J. Appl. Mech. 88 (5) (2021) 051009.
[20] M. Chen, W. Xu, Y. Liu, K. Yan, H. Jiang, Y. Wang, Band gap and double-negative properties of a star-structured sonic metamaterial, Appl. Acoust. 139 (2018) 235–242.
[21] J. Meng, Z. Deng, K. Zhang, X. Xu, F. Wen, Band gap analysis of star-shaped honeycombs with varied Poisson's ratio, Smart Mater. Struct. 24 (9) (2015) 095011.
[22] Z.-J. Wu, F.-M. Li, Spectral element method and its application in analysing the vibration band gap properties of two-dimensional square lattices, J. Vib. Control 22 (3) (2016) 710–721.
[23] Z.-J. Wu, F.-M. Li, C. Zhang, Vibration band-gap properties of three-dimensional Kagome lattices using the spectral element method, J. Sound Vib. 341 (2015) 162–173.
[24] S.-L. Zuo, F.-M. Li, C. Zhang, Numerical and experimental investigations on the vibration band-gap properties of periodic rigid frame structures, Acta Mech. 227 (2016) 1653–1669.
[25] Q. Lu, C. Liu, W. Yuan, W. Wei, F. Li, Vibration response and band gap characteristics of functionally graded frame structure, J. Vib. Control 28 (1–2) (2022) 230–239.
[26] L. Sun, J. Li, Y. Xiao, Broad and low frequency bandgap in truss core sandwich beam, Mech. Solids 56 (2021) 421–429.
[27] A.S. Phani, J. Woodhouse, N. Fleck, Wave propagation in two-dimensional periodic lattices, J. Acoust. Soc. Am. 119 (4) (2006) 1995–2005.
[28] N. Gao, Z. Wei, H. Hou, A.O. Krushynska, Design and experimental investigation of V-folded beams with acoustic black hole indentations, J. Acoust. Soc. Am. 145 (1) (2019) EL79–EL83.
[29] M.D. Nijs, Quantized Hall conductance in a two dimensional periodic potential, Phys. A: Stat. Mech. Appl. (1984).
[30] D. Malko, C. Neiss, F. Viñes, A. Görling, Competition for graphene: graphynes with direction-dependent dirac cones, Phys. Rev. Lett. 108 (8) (2012) 086804.
[31] F.D.M. Haldane, S. Raghu, Possible realization of directional optical waveguides in photonic crystals with broken time-reversal symmetry, Phys. Rev. Lett. 100 (1) (2008) 013904.
[32] S. Raghu, F.D.M. Haldane, Analogs of quantum-Hall-effect edge states in photonic crystals, Phys. Rev. A 78 (3) (2008) 033834.

[33] J. Lu, C. Qiu, L. Ye, X. Fan, M. Ke, F. Zhang, Z. Liu, Observation of topological valley transport of sound in sonic crystals, Nat. Phys. 13 (4) (2017) 369–374.
[34] C. He, X. Ni, H. Ge, X.-C. Sun, Y.-B. Chen, M.-H. Lu, X.-P. Liu, Y.-F. Chen, Acoustic topological insulator and robust one-way sound transport, Nat. Phys. 12 (12) (2016) 1124–1129.
[35] G. Zhang, Y. Gao, A three-dimensional magnetoelastic valley Hall insulator with tunable elastic wave route and frequency, J. Appl. Phys. 132 (22) (2022).
[36] Z. Huang, J.H. Wu, Y. Lei, C. Liu, F. Ma, Multi-band acoustic topological insulator, Mater. Today Phys. 27 (2022) 100793.
[37] Y. Xin, H. Wang, C. Wang, S. Cheng, Q. Zhao, Y. Sun, H. Gao, F. Ren, Properties and tunability of band gaps in innovative reentrant and star-shaped hybrid honeycomb metamaterials, Results Phys. 24 (2021) 104024.
[38] Q. Zhang, Y. Chen, K. Zhang, G. Hu, Dirac degeneracy and elastic topological valley modes induced by local resonant states, Phys. Rev. B 101 (1) (2020) 014101.
[39] L.-H. Wu, X. Hu, Scheme for achieving a topological photonic crystal by using dielectric material, Phys. Rev. Lett. 114 (22) (2015) 223901.
[40] Z. Huang, J. Wu, C. Wang, S. Yang, F. Ma, Resonant-scattering hybrid device for multiband acoustic topology valley transmission, Phys. Rev. B 104 (9) (2021) 094110.
[41] H. Zhang, B. Liu, X. Zhang, Q. Wu, X. Wang, Zone folding induced tunable topological interface states in one-dimensional phononic crystal plates, Phys. Lett. A 383 (23) (2019) 2797–2801.
[42] Z.-Y. Li, T.-X. Ma, Y.-Z. Wang, F.-M. Li, C. Zhang, Vibration isolation by novel meta-design of pyramid-core lattice sandwich structures, J. Sound Vib. 480 (2020) 115377.
[43] K. Modak, T.J. Saravanan, S. Rajasekharan, Dynamic analysis of coupled axial-bending wave propagation in a cracked timoshenko beam using spectral finite-element method, J. Vib. Eng. Technol. (2023) 1–23.
[44] Z. Yi, Z. Zhang, J. Huang, H. Xiang, C. He, L. Liu, Mechanism analysis and experimental verification of the bulging vibration characteristic of a fluid-solid metamaterial, Eng. Struct. 279 (2023) 115602.
[45] G. Hu, L. Tang, J. Xu, C. Lan, R. Das, Metamaterial with local resonators coupled by negative stiffness springs for enhanced vibration suppression, J. Appl. Mech. 86 (8) (2019) 081009.
[46] Z. Guo, J. Wen, D. Yu, G. Hu, Y. Yang, Widening the band gaps of hourglass lattice truss core sandwich structures for broadband vibration suppression, J. Vib. Acoust. Trans. ASME 145 (6) (2023) 061002.
[47] J. Deng, N. Gao, X. Chen, Ultrawide attenuation bands in gradient metabeams with acoustic black hole pillars, Thin-Walled Struct. 184 (2023) 110459.
[48] F. Ma, M. Huang, J.H. Wu, Acoustic metamaterials with synergetic coupling, J. Appl. Phys. 122 (21) (2017).
[49] X. Wang, Y. Pang, J.H. Wu, F. Ma, A broadband metamaterial damper design based on synergetic coupling among multi-cells, Appl. Acoust. 206 (2023) 109303.
[50] Y. Cai, J.H. Wu, Y. Xu, F. Ma, Realizing polarization band gaps and fluid-like elasticity by thin-plate elastic metamaterials, Compos. Struct. 262 (2021) 113351.